Supplementary Materials for:

# How much of the sediment in Gale crater's central mound was fluvially transported?

Bradley J. Thomson, Debra L. Buczkowski, Larry S. Crumpler, Kimberly D. Seelos, and Caleb I. Fassett

This PDF file includes:
Supplementary Text
Tables S1 to S4
Figures S1 to S5

## Supplementary Text

This supplementary section provides: (1) a description of the data used; (2) an expanded description of our methodology; (3) an explanation of the uncertainty analysis and error propagation, and (4) an expanded description of the paleotopography scenario. Supplementary tables and figures are appended to the end of the text.

**(1) Source Data:** We used topography data from the Mars Orbital Laser Altimeter (MOLA) instrument (Smith et al., 1999) and digital elevation models (DEMs) derived from High Resolution Stereo Camera (HRSC) stereo images (Neukum and Jaumann, 2004) to measure morphometric parameters of the Gale sedimentary mound and surrounding fluvial channels. MOLA data are collated into gridded products with a pixel spacing 463 m (equivalent to 128 pixels per degree) (Smith et al., 2003). The polar orbit of MOLA on Mars Global Surveyor resulted in a dense network of altimetry measurements at high latitudes, but equatorial gaps of up to ten km. As the crater Gale lies near the equator (it is centered at 5.4°S, 137.8°E), we used higher resolution HRSC DEMs supplement the MOLA gridded data. **Table S1** lists the HRSC DEMs used in this work. Four DEMs with a pixel spacing of 75 m cover the entire crater (**Fig. S1**) and a region to the west and constitute our main sources of topographic information; a higher resolution DEM (50 m pixel spacing) covers the western portion of the mound.

**(2) Methodology, valley network measurements:** First, the positions of valley networks required some manual adjustment (**Fig. S2**). *Hynek et al.* (2010) identified and mapped valley networks across Mars using THEMIS daytime infrared data mosaicked at 231 m/pixel supplemented with MOLA topography. Since this time, both uncontrolled (Edwards et al., 2011) and controlled 100 m/pixel THEMIS mosaics have been produced (Fergason et al., 2013), resulting in small offsets in the position of mapped features. Most features are only a few hundred meters offset from their previous mapped locations (typically 2-4 pixels), but some positional errors of up to 30 pixels or 3 km are apparent (Fergason et al., 2013).

Each mapped valley network segment was assigned a stream order (Strahler, 1957) by *Hynek et al.* (2010); these were slightly revised as appropriate. In this system, channels without tributaries are designated as 1st-order. Where two 1st-order channels join, the downstream segment is designated an order of 2; where two second-order channels join, a segment of order 3 is formed; and so forth. However, if two channels join that are of different order (e.g., a segment of order 1 merging with an order 2 segment), the order of the downstream segment is not incremented – it retains the highest order of the upstream channel segment. To assess the eroded volume in Farah Vallis and the upstream valley network, we measured segment shapes in a region to the southwest of

Gale that lies within HRSC DEM h1960_0000_da4. Profiles across selected channel segments were extracted from the DEM, and these were analyzed to determine the channel's cross-sectional area. The area was taken to be the difference between the current ground level and an assumed pre-erosional surface. **Table S2** provides a listing of all profiles collected and measured for this project. Three to four profiles were averaged together for each segment. As expected, lower-order channel segments typically have smaller cross-sectional areas than higher-order segments.

All cross-sectional area measurements of a given stream order (i.e., 1, 2, 3, or 4) were then combined using length-weighted median values that represent typical channel dimensions of each type (**Table S3**). The combined sum of these figures represents our estimate of total eroded volume of this valley network. One complicating factor is that for second-order valley network segments in particular, we observed that the choice of method for determining "typical" cross-sectional area values resulted in a notably large difference. As evidenced in the histogram below (**Figure S3**), the population of area values is distinctly bi-model. While the majority of areas are <0.1 $km^2$, a subset of larger features fall between 0.1 and 0.6 $km^2$. The median cross-sectional area is 0.12 $km^2$, near the low end of the range of values. The weighted, length-normalized median area is 0.36 $km^2$, which is a factor of three higher. To address this, we have computed the weighted median of 2nd order channel segments less than and greater than 0.1 $km^2$ separately. The weighted median of small channels is 0.0435 $km^2$, and the weighted median of large channels is 0.388 $km^2$. A simple average of these two weighted medians is 0.216 $km^2$, and this is the value we adopt in **Table S3**. A bar chart that summarizes the water-mobilized sediment volume compared to the mound volume is given in **Figure S4**.

**(3) Error propagation.** Our eroded valley network volume estimate is the sum of four products (equation S1):

$$V_{vn} = a_1L_1 + a_2L_2 + a_3L_3 + a_4L_4. \qquad \text{(S1)}$$

Here, $V_{vn}$ is the total cumulative volume of the valley network, $a_1$ to $a_4$ are the mean cross-sectional areas of stream order 1 to 4, respectively, and $L_1$ to $L_4$ are the total cumulative lengths of stream order types 1 to 4, respectively (**Table S3**). The uncertainty in $V_{vn}$ is dominated by the uncertainty in the mean areas; uncertainty in the length values is likely <1% and they are neglected in equation S2. The uncertainty in the volume calculation can be estimated using fractional uncertainties:

$$\delta V_{vn} = V_{vn}\sqrt{\frac{\delta a_1}{a_1} + \frac{\delta a_2}{a_2} + \frac{\delta a_3}{a_3} + \frac{\delta a_3}{a_3}} \qquad \text{(S2)}$$

In Eq. S2, $\delta a_1$ to $\delta a_3$ are the uncertainty in the cross-sectional area averages, taken here to be the standard deviations. This results in a formal uncertainty of $12.5\times10^3$ km$^3$, a value that is 150% larger than the volume of $8\times10^3$ km$^3$. Despite the fact that this valley network volume estimate is uncertain to within a factor of two, it is still almost an order of magnitude smaller than the mound volume (which approaches ~$10^5$ km$^3$).

The mound volume was determined by tabulating the difference between the current surface elevation and the assumed base elevation of -4.5 km, yielding a volume of 9414 km$^3$. To estimate the uncertainty in our estimate of the volume of the mound, we buffered the enclosed polygon that represents the mapped outermost extent of the mound (Thomson et al., 2011) one MOLA pixel (463 m) inward and outwards to obtain minimum (9301 km$^3$) and maximum (9520 km$^3$) error estimates, respectively. Thus we obtain our reported value of $9.4\pm0.1 \times 10^3$ km$^3$. However, there is an additional component of uncertainty related to the assumed base elevation surface under the Gale mound. Below we conduct a sensitivity analysis to explore how the mound volume (and by extension, the lower elevation level) varies given the choice of this parameter.

In the topographic profile of Gale given in **Figure S5**, the north-south topographic asymmetry of the crater is evident. The crater floor in the northern section of the crater lies more than 1 km deeper than the floor to the south of this crater. This asymmetry could be partly attributed to intrinsic factors such as Gale's formation on the northward-dipping dichotomy boundary or post-impact tilt, or it could reflect a depositional or erosional asymmetry that affected the infilling material.

We consider four potential base level surfaces to explore their effect on the volume calculations presented in this paper. First, we consider mound with a flat base at –4.5 km. Second, we consider a plane fit to the measured mound base elevation levels. Finally, following the approach of *Gabasova and Kite* (2018), we scale a radially averaged profile of a fresh example of complex martian crater (Tooting, 27.86 km in diameter) and a profile of a relatively fresh peak-ring crater (Galle, 223.5 km in diameter) to match the diameter of Gale using depth-diameter scaling relationships from *Tornabene et al.* (2013). These basal surfaces are given in **Fig. S5**; the resulting mound volumes are tabulated below.

As given in **Table S4**, three of the four basal surfaces considered (i.e., a flat plane, scaled Tooting crater, and scaled Galle basin) give reasonably consistent results, i.e., the volume of the mound is ~9.4 to $9.6\times10^3$ km$^3$. For the third basal surface considered, however, the mound volume is ~$6\times10^3$ km$^3$, which is about one-third less than the other cases. While this result does not alter the conclusion that the overwhelming majority of the mound in Gale is not attributable to aqueous transport processes, the elevation level that constitutes the boundary between the lower and intermediate elevation zone is more than 0.8 km higher than the other cases. Therefore, we consider this to be reflective the overall uncertainty associated with this elevation value. Accordingly, we have identified a range of elevation values on the mound in Figures 1 and 3.

**(4) Paleotopography scenario.**

Topography of the southern half of Gale was used to estimate the current average crater rim height of 0.58±0.41 km (Grotzinger et al., 2015). Based on measurements of other morphologically fresh craters between 40°S and 40°N (Robbins and Hynek, 2012), the initial rim height of Gale is estimated to have been ~1.6 km. The difference between the observed and expected rim height suggests ~1 km of net vertical erosion (Grotzinger et al., 2015), but the authors concede that this value is likely an overestimate based on preservation of Gale's ejecta blanket (Irwin et al., 2005). Using a geometric model of the potential sediment yield from this magnitude of wall erosion, Grotzinger et al. (2015) estimate that ~$9\times10^3$ $km^3$ of sediment could have delivered to the crater floor, a value that we note is roughly equivalent to the present-day mound volume. Assuming that the density of eroded and deposited material is the same (an assumption made by Grotzinger et al. [2015]), this yields 0.5 to 0.6 km of deposition over the 18,250 $km^2$ area of the crater floor, exclusive of the central peak region.

Based on rover observations of the exposed stratigraphy in Aeolis Mons, it also has been estimated that there was at least ~1 km of sediment present above the current crater floor that has since been eroded away (Grotzinger et al., 2015; Fedo et al., 2017). The preferred interpretation of the exposed stratigraphy is that it represents fluvial-deltaic deposits that undergo lateral facies transitions into fine-grained lacustrine deposits. The inferred sediment transport direction in these deposits is generally southward, i.e., toward the current mound, a geometry that would necessitate the presence of a now-eroded sequence of sediments in the gap between the crater walls and current mound.

The precise geometry of this now-eroded sedimentary sequence is necessarily speculative. The simplest configuration is to consider this volume of material spread uniformly from the crater wall toward central peak, accounting for a depth of 0.5 to 0.6 km of material (after Grotzinger et al., 2015). Additional sources of sediment considered in this current analysis collectively constitute ~$1.3\times10^3$ $km^3$, a volume that would account for a 70 m thick deposit if spread uniformly over the same area or about 300 m thick if tallied within the context of the existing mound topography. The lower elevation boundary would be –3.7 km in a flat plane is assumed for the basal boundary of the mound (**Table S5**).

There are several complicating factors with the deep burial and exhumation scenario. One paradoxical element of this scenario is that it would appear to require more sediment that visible means of transport into Gale would permit. Eolian processes such as the settling of dust or volcanic ash could be one potential mechanism that could contribute additional sediment into Gale. However, the grain-size segregation necessary to create the observed fine laminae is more likely in water, and therefore the settling of fine grains directly from the atmosphere “is excluded… … as a primary sediment accumulation mechanism [of the lower mound]” (Grotzinger et al., 2015). Evaporite sequences, perhaps delivered by groundwater, are another means to introduce material, but rover evidence suggests that the evaporitic material is pore-filling, not matrix-forming (e.g., Rampe et al., 2017).

The observed depth of Gale presents another potential complication to this scenario—local sediment sources and sinks inside the crater are out of balance by a factor of 2 to 4 in favor of the latter. Again using measurements of morphologically fresh craters (Robbins and Hynek, 2012), the initial depth of a crater Gale's size is estimated to have been 4.0 to 5.0 km; the current depth is 3.1±0.7 km (Grotzinger et al., 2015). The difference between the observed depth and expected depth range is 0.9 to 1.9 km, suggesting the crater has been shallowed by sedimentary infill. Yet the volume of sediment potentially shed from the walls is not sufficient to account for the inferred 1 to 2 km of shallowing.

Finally, two recent rover-based observations support the notional that former burial depths have been minimal in Gale. The first is observations that the compressive strength of rock drilled by the MSL rover range from very weak to medium strong (Peters et al., 2018). The presence of very weak rocks (i.e., with inferred compressive strengths ~5 MPa) is not straightforwardly compatible with deep burial and exhumation. Second, accelerometer data on MSL has been used to infer the near-surface density of the terrain over which the rover has traversed (Lewis et al., 2019). The inferred average density value of 1.680±0.180 g/cm$^3$ is low, and value indicates a high porosity (40±6%). As stated by Lewis et al., "This is a typical value for soils and poorly lithified sediments, but porosity is typically reduced in sedimentary rocks that have experienced burial and compaction."

**References cited in Supplementary Section**

Edwards, C. S., Nowicki, K. J., Christensen, P. R., Hill, J., Gorelick, N., and Murray, K., 2011, Mosaicking of global planetary image datasets: 1. Techniques and data processing for Thermal Emission Imaging System (THEMIS) multi‐spectral data: Journal of Geophysical Research, v. 116, no. E10008.

Fedo, C. M., et al., 2017, Facies Analysis and Basin Architecture of the Upper Part of the Murray Formation, Gale Crater, Mars, Lunar and Planetary Science Conference, Volume 48.

Fergason, R. L., Lee, E. M., and Weller, L., 2013, THEMIS geodetically controlled mosaics of Mars, Lunar and Planetary Science Conference, Volume 44: Houston, Texas, Lunar and Planetary Institute, p. abstract #1642.

Gabasova, L. R., and Kite, E. S., 2018, Compaction and sedimentary basin analysis on Mars: Planetary and Space Science, v. 152, p. 86-106.

Grotzinger, J. P., et al., 2015, Deposition, exhumation, and paleoclimate of an ancient lake deposit, Gale crater, Mars: Science, v. 350, no. 6257, p. aac7575.

Hynek, B. M., Beach, M., and Hoke, M. R. T., 2010, Updated global map of Martian valley networks and implications for climate and hydrologic processes: Journal of Geophysical Research, v. 115, p. 09008.

Irwin, R. P., Howard, A. D., Craddock, R. A., and Moore, J. M., 2005, An intense terminal epoch of widespread fluvial activity on early Mars: 2. Increased runoff and paleolake development: Journal of Geophysical Research, v. 110, p. E12S15.

Lewis, K. W., Peters, S., Gonter, K., Morrison, S., Schmerr, N., Vasavada, A. R., and Gabriel, T., 2019, A surface gravity traverse on Mars indicates low bedrock density at Gale crater: Science, v. 363, no. 6426, p. 535-537.

Neukum, G., and Jaumann, R., 2004, HRSC: The High Resolution Stereo Camera of Mars Express, *in* Wilson, A., ed., Mars Express: The Scientific Payload, Volume ESA Special Publication 1240, p. 17-35.

Peters, G. H., et al., 2018, Uniaxial compressive strengths of rocks drilled at Gale crater, Mars: Geophysical Research Letters, v. 45, p. 108-116.

Rampe, E., et al., 2017, Mineralogy of an ancient lacustrine mudstone succession from the Murray formation, Gale crater, Mars: Earth and Planetary Science Letters, v. 471, p. 172-185.

Robbins, S. J., and Hynek, B. M., 2012, A new global database of Mars impact craters≥ 1 km: 2. Global crater properties and regional variations of the simple‐to‐complex transition diameter: Journal of Geophysical Research, v. 117, no. E6.

Smith, D., Neumann, G., Arvidson, R. E., Guinness, E. A., and Slavney, S., 2003, Mars Global Surveyor Laser Altimeter Mission Experiment Gridded Data Record: NASA Planetary Data System.

Smith, D. E., et al., 1999, The global topography of Mars and implications for surface evolution: Science, v. 284, no. 5419, p. 1495-1503.

Strahler, A. N., 1957, Quantitative analysis of watershed geomorphology: Transactions, American Geophysical Union, v. 38, p. 913-920.

Thomson, B. J., et al., 2011, Constraints on the origin and evolution of the layered mound in Gale Crater, Mars using Mars Reconnaissance Orbiter data: Icarus, v. 214, p. 413-432.

Tornabene, L. L., Ling, V., Osinski, G. R., Boyce, J. M., Harrison, T. N., and McEwen, A. S., A revised global depth-diameter scaling relationship for Mars based on pitted impact melt-bearing craters, *in* Proceedings Lunar and Planetary Science Conference2013, Volume 44, p. abstract #2592.

**Table S1:** List of HRSC Digital Elevation Models (DEMs) of Gale and vicinity

| *HRSC product ID* | *Resolution (m)* | *Comments* |
|---|---|---|
| h1916_0000_da4 | 75 | Includes eastern portion of Gale |
| h1927_0000_da4 | 75 | Includes central portion of Gale |
| h1938_0000_da4 | 75 | Includes western portion of Gale |
| h1960_0000_da4 | 75 | Includes part of valley network SW of Gale |
| h5273_0000_da4 | 75 | Includes western half of Gale |
| h4235_0001_da4 | 50 | Includes western half of Gale |

**Table S2:** Valley network segment measurements

| *Object ID* | *Stream Order* | *Center Lat (°N)* | *Center Lon (°E)* | *Cross-sectional Area [km$^2$]* | *Segment Length [km]* | *Mean Area [km$^2$]* | *Std. Dev. [km$^2$]* |
|---|---|---|---|---|---|---|---|
| 454 a | 1 | -7.783 | 134.338 | 0.077 | 21.3 | 0.08 | 0.01 |
| 454 b | 1 | -7.861 | 134.401 | 0.092 | | | |
| 454 c | 1 | -7.924 | 134.456 | 0.073 | | | |
| 451 a | 1 | -7.730 | 134.746 | 0.060 | 13.0 | 0.11 | 0.07 |
| 451 b | 1 | -7.750 | 134.744 | 0.032 | | | |
| 451 c | 1 | -7.810 | 134.765 | 0.158 | | | |
| 409 a | 1 | -8.432 | 134.178 | 0.015 | 5.6 | 0.05 | 0.03 |
| 409 b | 1 | -8.453 | 134.193 | 0.070 | | | |
| 409 c | 1 | -8.481 | 134.202 | 0.058 | | | |
| 387 a | 1 | -8.823 | 134.106 | 0.057 | 21.5 | 0.18 | 0.20 |
| 387 b | 1 | -8.665 | 134.275 | 0.417 | | | |
| 387 c | 1 | -8.611 | 134.313 | 0.073 | | | |
| 390 a | 1 | -8.668 | 134.340 | 0.328 | 8.3 | 0.15 | 0.16 |
| 390 b | 1 | -8.646 | 134.340 | 0.083 | | | |
| 390 c | 1 | -8.600 | 134.322 | 0.040 | | | |
| 397 a | 1 | -8.611 | 134.599 | 0.111 | 12.3 | 0.11 | 0.01 |
| 397 b | 1 | -8.506 | 134.531 | 0.096 | | | |
| 397 c | 1 | -8.491 | 134.524 | 0.126 | | | |
| 518 a | 1 | -8.280 | 134.016 | 0.041 | 5.6 | 0.03 | 0.01 |
| 518 b | 1 | -8.275 | 134.043 | 0.033 | | | |
| 518 c | 1 | -8.491 | 134.524 | 0.014 | | | |
| 521 a | 1 | -8.187 | 134.057 | 0.023 | 6.6 | 0.04 | 0.03 |
| 521 b | 1 | -8.230 | 134.072 | 0.078 | | | |
| 521 c | 1 | -8.256 | 134.085 | 0.020 | | | |
| 520 a | 1 | -8.349 | 134.046 | 0.005 | 5.6 | 0.04 | 0.04 |
| 520 b | 1 | -8.340 | 134.081 | 0.083 | | | |
| 520 c | 1 | -8.321 | 134.091 | 0.019 | | | |
| 519 a | 1 | -8.372 | 134.095 | 0.048 | 7.5 | 0.05 | 0.03 |

| *Object ID* | *Stream Order* | *Center Lat (°N)* | *Center Lon (°E)* | *Cross-sectional Area [km²]* | *Segment Length [km]* | *Mean Area [km²]* | *Std. Dev. [km²]* |
|---|---|---|---|---|---|---|---|
| 519 b | 1 | -8.368 | 134.101 | 0.080 | | | |
| 519 c | 1 | -8.335 | 134.130 | 0.024 | | | |
| 408 a | 1 | -8.415 | 134.286 | 0.039 | 12.2 | 0.08 | 0.04 |
| 408 b | 1 | -8.371 | 134.321 | 0.096 | | | |
| 408 c | 1 | -8.316 | 134.335 | 0.118 | | | |
| 415 a | 1 | -8.339 | 134.418 | 0.053 | 9.5 | 0.06 | 0.01 |
| 415 b | 1 | -8.294 | 134.386 | 0.054 | | | |
| 415 c | 1 | -8.264 | 134.333 | 0.071 | | | |
| 430 a | 1 | -8.132 | 134.320 | 0.059 | 6.5 | 0.08 | 0.02 |
| 430 b | 1 | -8.154 | 134.355 | 0.097 | | | |
| 430 c | 1 | -8.186 | 134.369 | 0.088 | | | |
| 402 a | 2 | -8.477 | 134.268 | 0.525 | 20.4 | 0.45 | 0.08 |
| 402 b | 2 | -8.390 | 134.362 | 0.452 | | | |
| 402 c | 2 | -8.450 | 134.465 | 0.368 | | | |
| 395 a2 | 2 | -8.594 | 134.039 | 0.334 | 46.5 | 0.39 | 0.06 |
| 395 b | 2 | -8.512 | 134.166 | 0.388 | | | |
| 395 c | 2 | -8.515 | 134.193 | 0.461 | | | |
| 399 a | 2 | -8.566 | 134.318 | 0.149 | 14.3 | 0.25 | 0.12 |
| 399 b | 2 | -8.542 | 134.388 | 0.384 | | | |
| 399 c | 2 | -8.521 | 134.414 | 0.219 | | | |
| 522-523 a | 2 | -8.293 | 134.098 | 0.056 | 4.2 | 0.06 | 0.02 |
| 522-523 b | 2 | -8.307 | 134.101 | 0.085 | | | |
| 522-523 c | 2 | -8.316 | 134.113 | 0.040 | | | |
| 522-523 d | 2 | -8.321 | 134.128 | 0.071 | | | |
| 420 a | 2 | -8.324 | 134.143 | 0.204 | 12.9 | 0.35 | 0.14 |
| 420 b | 2 | -8.326 | 134.179 | 0.479 | | | |
| 420 c | 2 | -8.285 | 134.269 | 0.358 | | | |
| 516 a | 2 | -8.105 | 134.455 | 0.044 | 8.0 | 0.04 | 0.02 |
| 516 b | 2 | -8.084 | 134.477 | 0.057 | | | |
| 516 c | 2 | -8.059 | 134.513 | 0.036 | | | |
| 516 d | 2 | -8.039 | 134.513 | 0.011 | | | |
| 422-424 a | 2 | -8.233 | 134.312 | 0.089 | 5.3 | 0.08 | 0.03 |
| 422-424 b | 2 | -8.207 | 134.345 | 0.043 | | | |
| 422-424 c | 2 | -8.197 | 134.363 | 0.098 | | | |
| 426-427-438 a | 2 | -8.185 | 134.393 | 0.023 | 7.9 | 0.10 | 0.13 |
| 426-427-438 b | 2 | -8.171 | 134.422 | 0.037 | | | |
| 426-427-438 c | 2 | -8.123 | 134.442 | 0.252 | | | |
| 404-405 a | 3 | -8.477 | 134.500 | 0.230 | 29.1 | 0.30 | 0.14 |
| 404-405 b | 3 | -8.448 | 134.588 | 0.192 | | | |
| 404-405 c | 3 | -8.309 | 134.630 | 0.509 | | | |
| 404-405 d | 3 | -8.156 | 134.639 | 0.268 | | | |
| 524 a | 3 | -8.037 | 134.545 | 0.110 | 8.1 | 0.15 | 0.04 |
| 439 b | 3 | -8.072 | 134.592 | 0.159 | | | |
| 529 c | 3 | -8.084 | 134.616 | 0.179 | | | |
| 528 a | 4 | -8.057 | 134.662 | 0.223 | 6.2 | 0.28 | 0.09 |
| 528 b | 4 | -8.039 | 134.684 | 0.237 | | | |
| 528 c | 4 | -8.038 | 134.716 | 0.377 | | | |
| 429 a | 4 | -8.062 | 134.753 | 0.400 | 16.1 | 0.27 | 0.12 |
| 429 b | 4 | -8.116 | 134.792 | 0.165 | | | |
| 429 c | 4 | -8.148 | 134.832 | 0.234 | | | |
| 431 a | 4 | -8.139 | 134.966 | 0.466 | 6.4 | 0.63 | 0.29 |
| 431 b | 4 | -8.121 | 134.994 | 0.456 | | | |
| 431 c | 4 | -8.097 | 135.005 | 0.965 | | | |

| *Object ID* | *Stream Order* | *Center Lat (°N)* | *Center Lon (°E)* | *Cross-sectional Area [km$^2$]* | *Segment Length [km]* | *Mean Area [km$^2$]* | *Std. Dev. [km$^2$]* |
|---|---|---|---|---|---|---|---|
| 432 a | 4 | -8.097 | 135.053 | 0.307 | 53.5 | 0.21 | 0.09 |
| 432 b | 4 | -8.013 | 135.235 | 0.154 | | | |
| 432 c | 4 | -7.999 | 135.276 | 0.158 | | | |

**Table S3:** Cumulative volume by stream order

| *Stream Order* | *Normalized Median Area [km$^2$]* | *Stand. Dev. [km$^2$]* | *Total Length [km]* | *Volume [km$^3$]* |
|---|---|---|---|---|
| 1 | 0.07 | 0.08 | 2970 | 218 |
| 2 | 0.22 | 0.17 | 1203 | 260 |
| 3 | 0.23 | 0.13 | 574 | 132 |
| 4 | 0.31 | 0.21 | 645 | 198 |
| | | | | Total Cumulative Volume [km$^3$] |
| | | | | 808 |

**Table S4:** Gale basal elevation options with modern topography given in Fig. S4

| *Assumed basal topography* | *Current mound volume [km$^3$]* | *Lower elevation level [km]* | *Ratio volume moved by water to mound volume* | *Fraction of volume moved by water* |
|---|---|---|---|---|
| Flat base | 9410 | –4.21 | 1 : 7.54 | 13.3% |
| Inclined plane | 6070 | –3.47 | 1 : 4.87 | 20.5% |
| Tooting crater, scaled | 9480 | –4.25 | 1 : 7.59 | 13.2% |
| Galle basin, scaled | 9630 | –4.27 | 1 : 7.71 | 13.0% |

**Table S5:** Gale basal elevation options with inferred paleotopography

| *Assumed basal topography* | *Mound paleovolume [km$^3$]* | *Lower elevation level [km]* |
|---|---|---|
| Flat base | 18400 | –3.67 |
| Inclined plane | 15100 | –3.34 |
| Tooting crater, scaled | 18500 | –3.66 |
| Galle basin, scaled | 18600 | –3.67 |

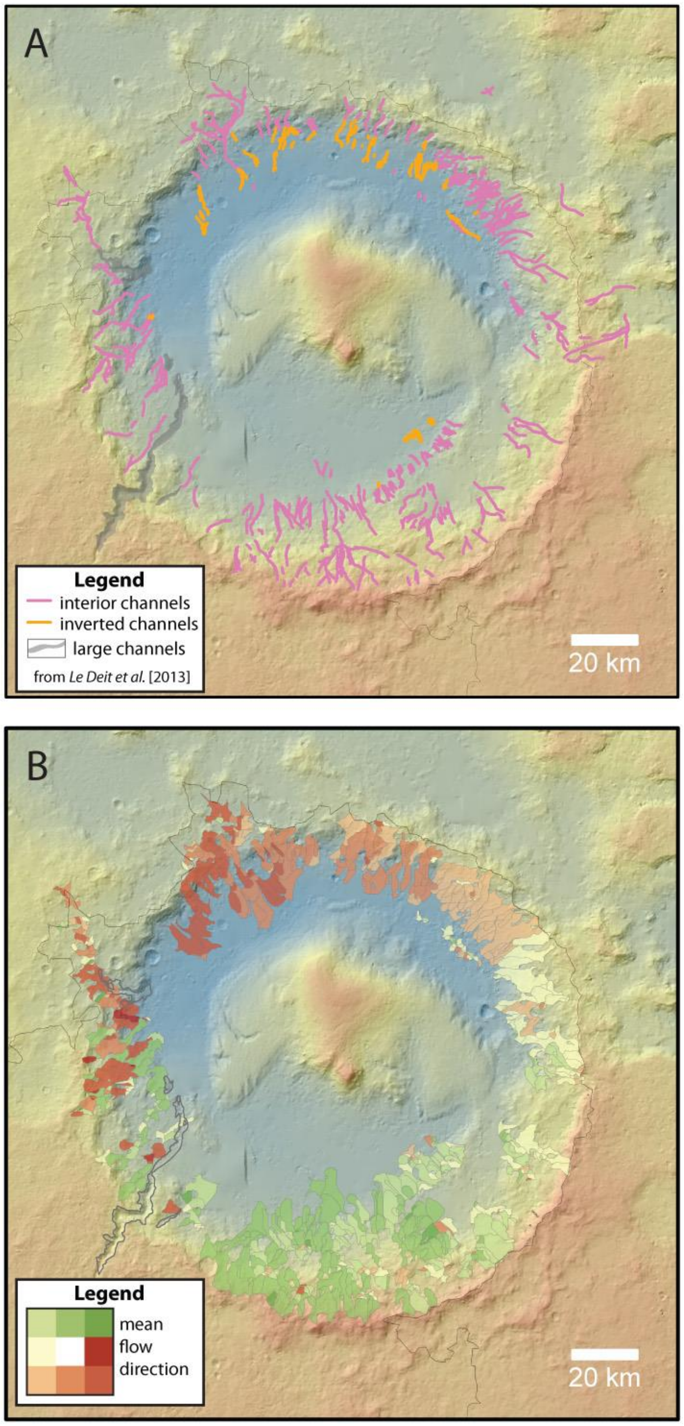


**Figure S1.** Shaded relief map of Gale crater from HRSC-derived topography. **(a)** Interior channels and inverted channels are given in pink and orange respectively [from *Le Deit et al.*, 2013]; larger inward-draining channels are outlined in gray. **(b)** Same view as Fig. 1a indicating sub-divided interior watersheds. The N=705 separate watersheds are assigned colors based on their mean flow direction.

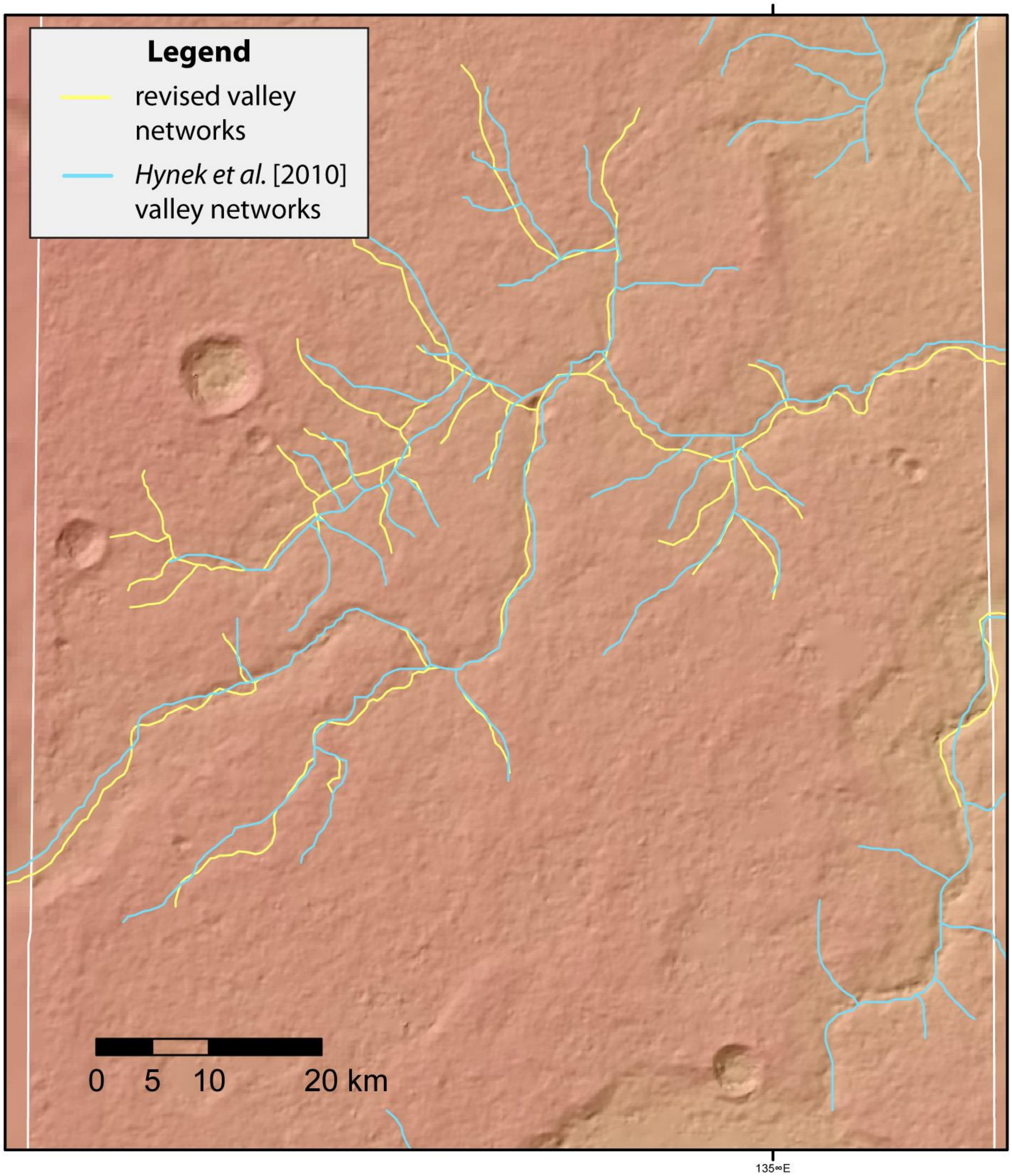


**Figure S2.** Comparison of valley networks mapped by Hynek et al (2010) (given in blue) with those re-mapped in this study (given in yellow). White border marks extent of HRSC DEM H1960_0000; background is MOLA shaded relief map.

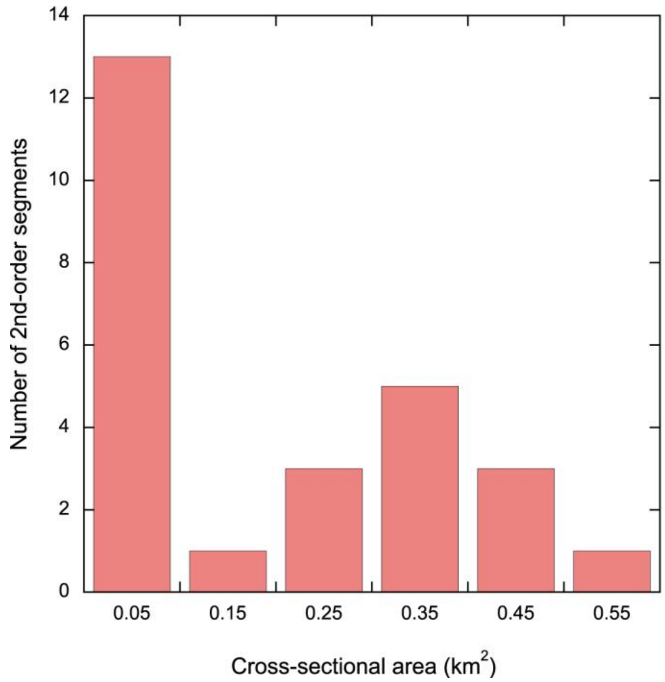


**Figure S3.** Histogram of the cross-sectional areas of second-order valley network segments. X-axis labels are bin centers; tick marks are at increments of 0.1 km$^2$.

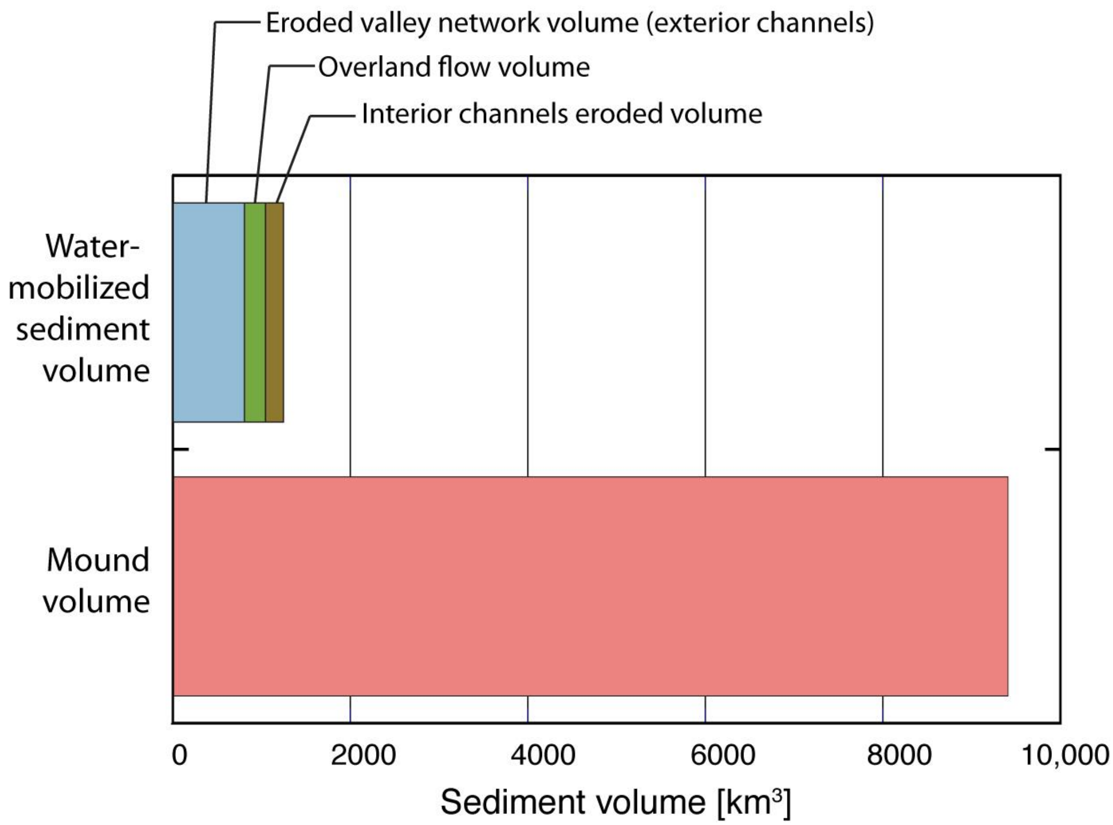


**Figure S4.** Comparison of the volume of sediment mobilized by water with the total volume of sediment in the mound.

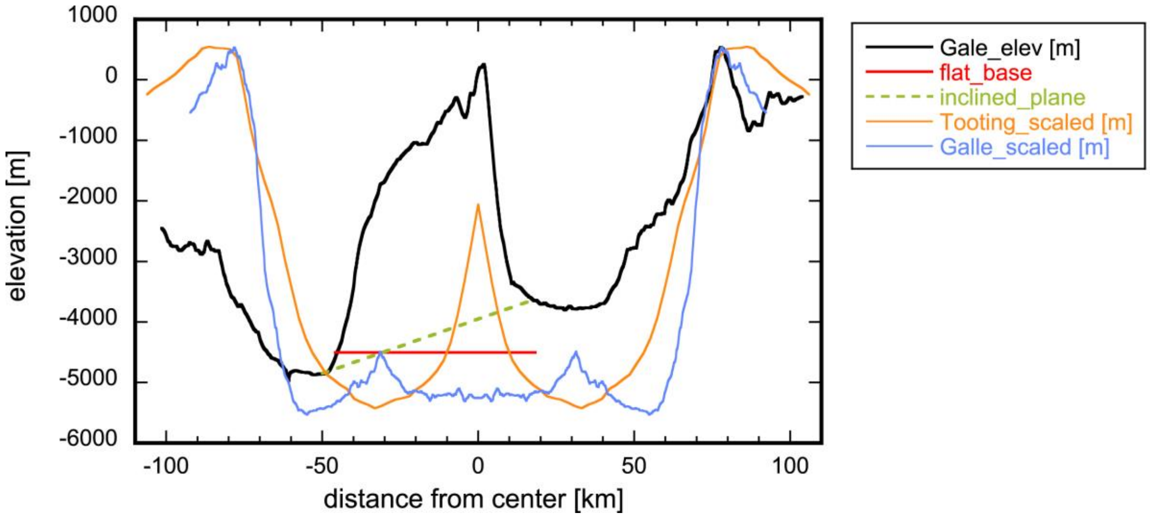


**Figure S5.** Two-segment topographic profile of Gale crater from north to south in black. Given in red is flat base elevation level of –4.5 km; the dashed green line is an inclined plane fit the mound base. The orange and blue curves are radially averaged profiles of Tooting crater and the Galle basin, respectively, from *Gabasova and Kite* (2018) that were scaled to Gale's diameter (*Tornabene et al.*, 2013).